A method to correct for the effect of blockage and wakes on power performance measurements

Alessandro Sebastiani[1], James Bleeg[2], and Alfredo Peña[1]

[1]DTU Wind and Energy Systems, Frederiksborgvej 399, 4000 Roskilde, Denmark
[2]DNV, One Linear Park, Avon St, Temple Quay, Bristol BS2 0PS, UK

Correspondence: Alessandro Sebastiani (aseb@dtu.dk)

Abstract.

Wind turbine power performance measurements often occur at the perimeter of a wind farm, where the wind flow is subject to blockage effects, which might impact the measured power performance. We perform Reynolds-averaged Navier-Stokes simulations of a wind farm with five rows of twenty turbines each, operating in a conventionally neutral boundary layer, to evaluate
5   whether the power performances measured for turbines in the upstream row would differ from that of a turbine operating in isolation under the same inflow conditions. We simulate the power performance measurements with both meteorological masts and nacelle-mounted lidars. Results show that blockage effects have an impact on the measured power performance of the wind farm turbines, with measured power coefficient varying more than 1% relative to what is measured for the isolated turbine. In this work, we propose a method to correct for the effect of blockage on power performance measurements, yielding a curve that
10 is more consistent with how power curves in energy yield analyses are defined and used, and thereby allowing for more useful comparisons between these curves. Our numerical results indicate that the correction method greatly reduces blockage-related variance and bias in the measured power curves. While flow modelling can be used to calculate the correction factors for actual power performance measurements in the field, we additionally show how some of the correction factors can be derived from lidar measurements. Finally, the numerical results suggest that the method could also be used to correct for the effect of wakes
15 on power performance measurements conducted on turbines located downstream of the leading row.

1   Introduction

Wind turbine power curve measurements play an important role in the wind industry. Manufacturers use them to better understand the performance of their fleet of operating turbines, and also to refine their power predictions for new, untested designs. Wind farm owners use on-site power performance measurements to determine whether their turbines are performing at a level
20 consistent with the predicted, theoretical power curves provided by the manufacturer. The vast majority of power performance measurements are conducted in wind farms for this purpose. Any assessment of discrepancies between actual wind farm energy production and the pre-construction estimate is not complete without verification of turbine power performance.

In an energy yield analysis, theoretical turbine power curves are the key link between the expected freestream wind resource and the predicted energy production of a planned wind farm. As such, theoretical power curves are traditionally defined as

functions of hub-height freestream wind speed. When running a power performance verification test, it is straightforward to measure the power; however, the freestream wind speed—i.e. the horizontal wind speed that would prevail at the turbine location if the wind turbine was not there—is not a measurable quantity. Instead, power performance measurement campaigns are designed to measure a wind speed that is expected to be very close to what the hub-height freestream wind speed would be if we could measure it. The IEC standard for power performance measurements (IEC, 2017) requires the mast or lidar to

30 measure between two and four rotor diameters (D) upstream of the test turbine, close enough for the flow to be well correlated with conditions at the turbine, but far enough, ostensibly, for the influence of turbine induction on the measured wind speed to be negligibly small. In addition, the measurement location and valid wind directions are restricted to avoid upstream wakes. The IEC standard states the purpose of these requirements clearly (IEC, 2017): "The WME (wind measurement equipment) shall not be influenced by the wind turbine under test. The wind turbine under test and the WME shall not be influenced by

35 neighbouring operating wind turbines."

Despite these restrictions, there is growing evidence that turbine-related disturbances materially influence power performance measurements. The most compelling evidence involves field observations. Nacelle-mounted lidar measurements at eight different offshore wind farms reported by Nygaard and Brink (2017) showed that the wind speeds measured 2.5D upstream of the test turbines were below freestream, an average of 1.0% below according to their estimate. Based on this finding,

40 they recommended applying an "induction correction factor" when calculating energy yield using a measured power curve or similarly productive theoretical curve. Using meteorological mast measurements taken before and after the start of operation at three onshore wind farms, Bleeg et al. (2018) found that wind speeds measured 2D upstream the wind farms decreased by 3.4%, on average, relative to wind speeds measured farther away after the turbines started operating. The observed slowdowns were well in excess of what could be attributed to induction of a single turbine, which in part led to the conclusion that the

45 other wind farm turbines also contributed to these slowdowns. Based on additional analysis, they further concluded that wind farm blockage not only reduces the wind speed upstream of the wind farm, but it also reduces the wind speed experienced by the turbines on the upstream perimeter of the wind farm, causing them to generally produce less than they would operating in isolation. An analysis of power performance measurements conducted in a row of five turbines, along with a complementary set of Reynolds-Averaged Navier-Stokes (RANS) simulations, showed that wind farm blockage materially influences the mea-

50 surements (Sebastiani et al., 2022). Specifically, wind farm blockage appears to affect the wind speed relationship between the mast location and the rotor in these results. Beyond field observations, there are also simulation-based studies (Allaerts and Meyers, 2017; Meyer Forsting et al., 2017; Nishino and Draper, 2015; Strickland and Stevens, 2022) and wind tunnel studies (Medici et al., 2011; Ebenhoch et al., 2017; Segalini and Dahlberg, 2020; McTavish et al., 2015) that highlight turbine-related flow disturbances that likely affect power performance measurements.

55 The IEC standard explains how to correct for flow distortions caused by terrain, but there is nothing on how to correct for flow disturbances/distortions caused by wind turbines. Although there is emerging recognition that turbine-induced flow disturbances should be accounted for, the wind energy community at present lacks a generally accepted method to quantify the impact of these flow disturbances and thereby correct for them. Specifically, although several models have been developed to

account for blockage effects on turbine interaction loss (Nygaard et al., 2020; Branlard and Meyer Forsting, 2020; Segalini, 2021; Bleeg, 2020), but accounting for blockage effects on power performance measurements is still a rather unexplored topic.

Here, we propose a method to correct for the impact of turbine-related disturbances on power performance measurements. The methodology, which applies to both mast- and lidar-based measurements, is designed to yield power curves that are consistent with how theoretical curves are defined. After describing the correction method in detail, including the reasoning behind it, we test the method using RANS simulations of a notional wind farm. Finally, we explore whether the correction can be completed, at least partly, using nacelle lidar measurements rather than flow simulations alone.

The work is organized as follows. In Sect. 2, the correction method is explained. In Sect. 3, the numerical model is presented with descriptions of the computational fluid dynamics (CFD) model (Sect. 3.1), the simulation set-up (Sect. 3.2) and the virtual lidar measurements (Sect. 3.3). Results from power performance measurements conducted on the first upstream row of a wind farm are shown in Sect. 4, while in Sect. 5 we show how short-range nacelle lidar measurements can be used to apply the correction method. In Sect. 6, the correction method is applied to all turbines in the wind farm, including downstream waked turbines. Finally, discussion and conclusions are presented in Sects. 7 and 8, respectively.

2   Correction method

Common practice, when estimating the energy yield of a planned wind farm, is to combine the expected freestream wind resource at each turbine location with the manufacturer-provided theoretical power curve to calculate the so-called gross energy. This is the total of the energy that each turbine would produce absent the presence of the other wind turbines and other loss sources. The net energy is obtained after turbine interaction and other losses are accounted for. Thus, the power curve used in an energy yield analysis should faithfully represent the power production of the turbine as function of freestream wind speed when the turbine is operating in isolation. We refer to this power curve definition as a freestream power curve, $P(U_\infty)$.

A power curve measured according to IEC standards, $P(U_{\mathrm{mast}})$, is not a freestream power curve as defined above. The test turbine affects the measured wind speed via induction, and the other wind farm turbines affect the relationship between that wind speed and conditions at the rotor face, via blockage and sometimes wakes. The impact of these effects on the measured power curve should be quantified and corrected. The objective of the correction method described in this section is to convert the measured power curve to a freestream curve that can defensibly be compared with a theoretical power curve. In our approach, we only alter the wind speed column in the tabular power curve. Specifically, for a given measured power vs. wind speed pair in the table, we correct to the freestream mean wind speed that would prevail if the test turbine were producing the same amount of power while operating in isolation. The correction can be thought of a two-step process:

- Convert the measured curve to what would be measured if the test turbine were operating in isolation and producing the same amount of power measured in the test.

- Correct for the impact of induction from the isolated turbine on the mast wind speed.

90   When measuring the power performance of a turbine inside a wind farm, the measured power curve $P^{\mathrm{WF}} = P(U_{\mathrm{mast}}^{\mathrm{WF}})$ differs

from the power curve that would be measured if the turbine were operating in isolated condition $P^{\mathrm{I}} = P(U_{\mathrm{mast}}^{\mathrm{I}})$, since both P

and U_{mast} are affected by surrounding turbines. Consequently, since both power and wind speed are different ($P^{\mathrm{WF}} \neq P^{\mathrm{I}}$ and

$U_{\mathrm{mast}}^{\mathrm{WF}} \neq U_{\mathrm{mast}}^{\mathrm{I}}$), both $U_{\mathrm{mast}}^{\mathrm{WF}}$ and P^{WF} should be corrected in order to retrieve the power performance of the isolated turbine

from wind farm measurements. However, if we consider the case with the isolated and the wind farm turbines producing the

95   same amount of power $P = P^{\mathrm{I}} = P^{\mathrm{WF}}$, we would only need to correct the wind speed measurement, retrieving $U_{\mathrm{mast}}^{\mathrm{I}}$ from

$U_{\mathrm{mast}}^{\mathrm{WF}}$.

Although wind turbine power is commonly formulated as a function of freestream wind speed, it is more directly a function

of the velocity across the rotor face, which, along with air density and rotor speed, determines the aerodynamic loads on the

blades. In this paper, we use the average axial velocity across the rotor face as a power-equivalent wind speed, U_{disk}. In other

100   words, if two turbines experience the same U_{disk}, they are assumed to produce the same amount of power regardless of the

respective U_{mast} and U_{∞} values. Thus, if $P^{\mathrm{I}} = P^{\mathrm{WF}}$, then $(U_{\mathrm{disk}}^{\mathrm{I}}/U_{\mathrm{disk}}^{\mathrm{WF}}) = 1$, and $U_{\mathrm{mast}}^{\mathrm{I}}$ can be reconstructed from $U_{\mathrm{mast}}^{\mathrm{WF}}$ as

$$U_{\mathrm{mast}}^{\mathrm{I,rec}} = U_{\mathrm{mast}}^{\mathrm{WF}} \left(\frac{U_{\mathrm{disk}}}{U_{\mathrm{mast}}} \right)^{\mathrm{WF}} \left(\frac{U_{\mathrm{mast}}}{U_{\mathrm{disk}}} \right)^{\mathrm{I}}, \tag{1}$$

where $U_{\mathrm{mast}}^{\mathrm{I,rec}}$ is the reconstructed velocity at the mast of the isolated turbine, $U_{\mathrm{mast}}^{\mathrm{WF}}$ is the velocity measured at the wind-farm

mast, and the ratios $(U_{\mathrm{disk}}/U_{\mathrm{mast}})^{\mathrm{WF}}$ and $(U_{\mathrm{mast}}/U_{\mathrm{disk}})^{\mathrm{I}}$ are computed from numerical simulations of the wind farm and the

105   isolated turbine, respectively.

The ratio $(U_{\mathrm{mast}}/U_{\mathrm{disk}})^{I}$ relates to the turbine blockage/induction and can be assumed to be nearly constant with small

changes in wind speed over the plateau of the thrust-coefficient curve $C_T = C_T(U_{\infty})$. Therefore, Eq. (1) is still valid in the

case of $U_{\mathrm{disk}}^{\mathrm{WF}} \neq U_{\mathrm{disk}}^{\mathrm{I}}$, as long as the turbine is operating at nearly the same thrust coefficient $C_T = C_T^{\mathrm{WF}} = C_T^{\mathrm{I}}$ and at a similar

wind speed.

110   When $U_{\mathrm{mast}}^{\mathrm{I}}$ is retrieved at a distance of 2D upstream of the rotor, it might be affected by turbine blockage. Therefore, a

similar approach as that used to derive Eq. (1) can be applied to reconstruct the freestream velocity:

$$U_{\infty}^{\mathrm{rec}} = U_{\mathrm{mast}}^{\mathrm{I,rec}} \left(\frac{U_{\infty}}{U_{\mathrm{mast}}} \right)^{\mathrm{I}}, \tag{2}$$

where $U_{\mathrm{mast}}^{\mathrm{I,rec}}$ is given by Eq. (1) and $(U_{\infty}/U_{\mathrm{mast}})^{\mathrm{I}}$ is computed from simulations of both the isolated turbine and the undis-

turbed free flow.

115   Some variations are expected for both $(U_{\mathrm{mast}}/U_{\mathrm{disk}})^{\mathrm{I}}$ and $(U_{\infty}/U_{\mathrm{mast}})^{\mathrm{I}}$ depending on the wind direction, as the degree

of blockage at the mast depends on turbine yaw. Therefore, we also simulate IEC-compliant measurements with a 2-beam

nacelle-mounted lidar, which yaws with the turbine. In those cases, we refer to the IEC wind speed measurement as either

$U_{\mathrm{lidar}}^{\mathrm{I}}$ or $U_{\mathrm{lidar}}^{\mathrm{WF}}$.

3 Numerical model

3.1 CFD model

120

The numerical simulations are run using a CFD model based on STAR-CCM+, a general-purpose CFD software. The model solves the steady-state RANS equations along with a transport equation for potential temperature. The turbulence model is standard $k - \epsilon$ with modified coefficients. Buoyancy effects are captured through the addition of a gravity term in the vertical momentum equation, which is formulated using a shallow Boussinesq approximation. Buoyancy source terms are also included

125 in the turbulence equations. More details about the flow model may be found in Bleeg et al. (2015b) and Bleeg et al. (2015a).

The turbines are represented via an actuator disk model. The disk volumes are discretised with cubic mesh cells with edge lengths equal to 5% of the rotor diameter (20 cells across the rotor diameter and 5 cells across the disk thickness). The axial and tangential body forces applied to the disk are modelled as a function of the disk-averaged axial velocity at the rotor face when the turbine is operating (U_{disk}). Since manufacturer-provided curves for power and thrust coefficient (C_T) are functions

130 of freestream wind speed (U_∞), the curves used in the simulations need to be reformulated to be functions of U_{disk}. The conversion of the manufacturer-provided C_T and power curves follows a procedure similar to that of van der Laan et al. (2015). The procedure involves running a series of single-turbine simulations, each corresponding to a different hub-height wind speed. In these simulations, the U_∞ values are known, and actuator disk forces are thereby set according to theoretical curves specified as functions of U_∞. After each simulation finishes, we record U_{disk}. The outcome of the conversion is a set of

135 curves ($P'(U_{\mathrm{disk}})$, $C_T'(U_{\mathrm{disk}})$, and rotor speed) specified as a function of U_{disk}.

All simulations correspond to a conventionally neutral boundary layer with a thickness of approximately 1000 m. The maximum potential gradient in the capping inversion is 10 K/km, and the free atmosphere above is stably stratified with a vertical potential temperature gradient of 3.3 K/km. In this numerical experiment, three types of simulations are run: full wind farm, turbines in isolation, and freestream. As the labels imply, the full wind farm simulations include all the wind turbines,

140 the isolated turbine simulations only include one turbine, and the freestream simulations have no turbines/actuator disks. The three types of simulations are run with the same mesh and boundary conditions.

3.2 Simulation set-up

We perform RANS simulations of a wind farm with five rows of 20 turbines, as shown in Fig. 1-(a). The turbines have a rotor diameter of 136 m and are distributed with spacings of 3D and 10D along the x and y directions, respectively. We simulate

145 five different wind directions, covering the sector from $-45°$ to $+45°$ with respect to the orthogonal wind direction $\theta = 0°$ as shown in Fig. 1-(a). The turbines are numbered starting from the most downwind row, so that turbines from T81 to T100 are wake-free for all the simulated wind directions.

Simulations are also performed with a single turbine operating within the same domain and under the same free-flow conditions of the wind farm. We simulate four different single-turbine cases in order to evaluate whether numerical effects cause

150 different results for the isolated turbine when this is placed at different locations. We simulate the single turbine at the locations of T28, T81, T92 and T100 and, although not shown, we find that the results are independent of the location of the isolated

turbine. Therefore, in the following analysis, when we refer to the case with the isolated turbine, we point at the isolated turbine at T92, as shown in Fig. 1-(b).
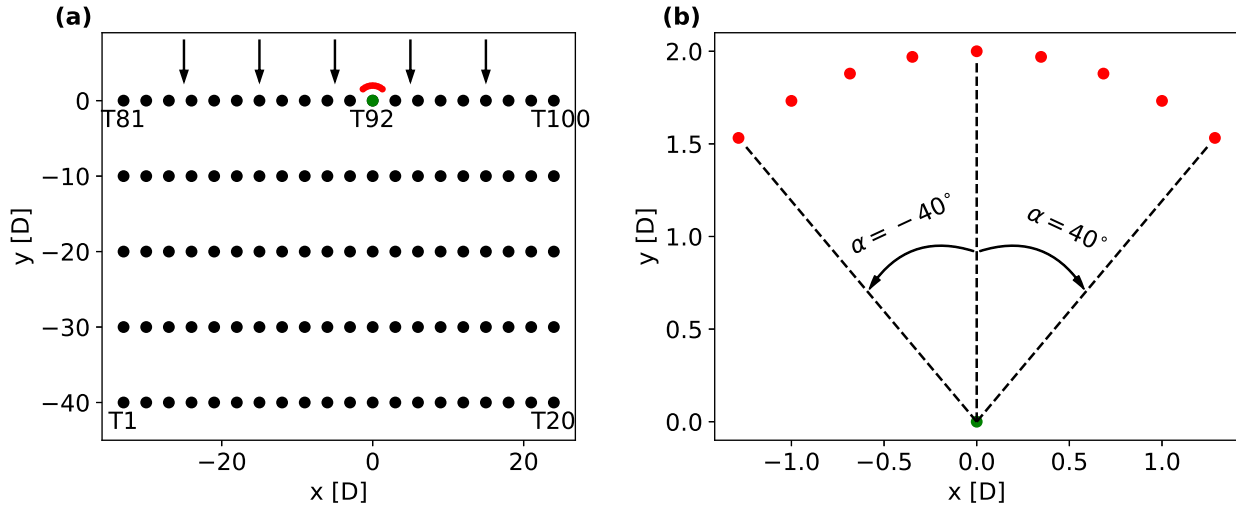
Figure 1. Illustrations of the wind farm layout (a) and the isolated turbine (b), with both wind turbine (*black circles*) and mast (*red circles*) locations. The arrows in (a) show the $\theta = 0°$ wind direction.

To test the correction method, i.e., Eqs. (1) and (2), we extract the wind speed at hub height in front of all the first-row turbines
155 in the full wind farm simulation and in front of the the isolated turbine simulation. To test all the possible IEC-compliant wind speed measurements, we simulate nine masts located on the 2D-radius circle around each turbine and distributed every $10°$ from $\alpha = -40°$ to $\alpha = 40°$ relatively to the north, as shown in Fig. 1-(b). It should be noted that, according to the IEC standard, the available sector for power performance tests for the full wind farm simulation would be larger than $[-40°, +40°]$ for the locations of T81 and T100, as there are no neighbouring turbines on one or both sides of these locations. However, to keep
160 consistency in the comparison between the 20 upstream turbines and the isolated turbine, we consider the same sector of $-40°$ to $40°$ for all these turbine locations.

We aim to simulate five wind directions regularly distributed over the $[-45°, +45°]$ interval. However, the simulated flow field is characterized by vertical veer due to the combination of surface friction and Coriolis force, so the wind direction varies around $4°$ from bottom to top of the rotor swept area, as shown in Fig. 2-(b), with wind directions at hub height of $-46°$, $-23°$,
165 $-1°$, $20°$ and $44°$. Additionally, Fig. 2-(a) shows the vertical velocity profiles, which are all characterized by a horizontal wind speed of around 7.1 m/s at hub height, with variations from ∼5.9 to ∼7.8 m/s across the rotor swept area. The wind speed was chosen so that the all the simulated turbines operate on the plateau of the C_T curve.
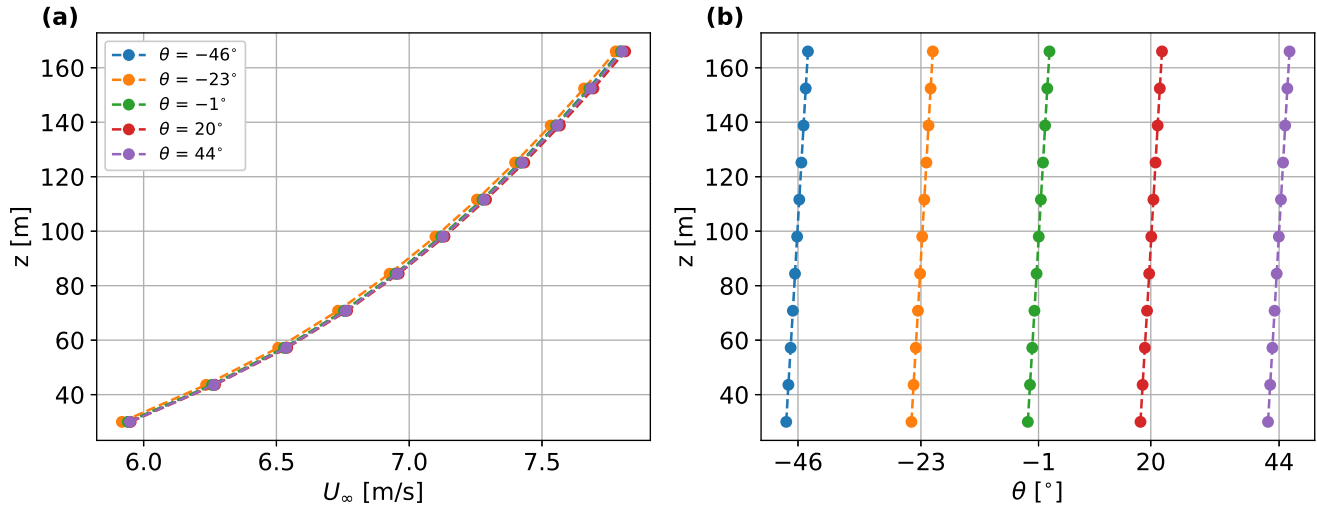
Figure 2. Vertical profiles of the horizontal wind speed (a) and wind direction (b) extracted at the location of T92 from the freestream simulations.

3.3 Virtual lidar measurements

The correction method is based on the combination of measurements (U_{mast} or U_{lidar}) with the numerically computed value
170 of U_{disk}, which is hard to estimate out in the field. Therefore, we investigate whether U_{disk} can be replaced with a measurable velocity quantity: we simulate short-range nacelle lidar measurements in the induction zone and derive a velocity quantity $U_{\text{disk,lidar}}$ that is tested as a proxy for U_{disk} in Eq. (1). Furthermore, we simulate IEC-compliant nacelle lidar measurements to evaluate the performance of the correction method when replacing U_{mast} with U_{lidar} in Eq. (1).

We retrieve the IEC-compliant wind speed measurements with a 2-beam nacelle-mounted lidar measuring at 2D upstream of
175 the rotor with a half-opening angle $\varphi = 15°$. Additionally, as shown in Fig. 3, we retrieve wind speed values at 0.5D upstream of the rotor with four different nacelle lidars: the same 2-beam lidar used to measure at 2D; a 4-beam lidar with $\varphi = 18°$ and the measurement points at the four vertices of a square; a 50-beam circularly scanning lidar with $\varphi = 15°$; and an additional 50-beam ideal lidar that scans along the circular pattern of radius equal to three quarters of the rotor radius. The choice of the 50-beam ideal lidar scanning pattern is based on the work by Sebastiani et al. (2023), who showed that, among several circular
180 scanning patterns, the one scanning at around a three quarter of the radius provided the highest accuracy in power prediction.

We assume horizontal homogeneity of the flow field to reconstruct the horizontal wind speed at hub height from the 2-beam lidar measurements by inverting the linear system

$$\begin{pmatrix} n_x^1 & n_y^1 \\ n_x^2 & n_y^2 \end{pmatrix} \cdot \begin{pmatrix} u_x \\ u_y \end{pmatrix} = \begin{pmatrix} v_r^1 \\ v_r^2 \end{pmatrix}, \tag{3}$$
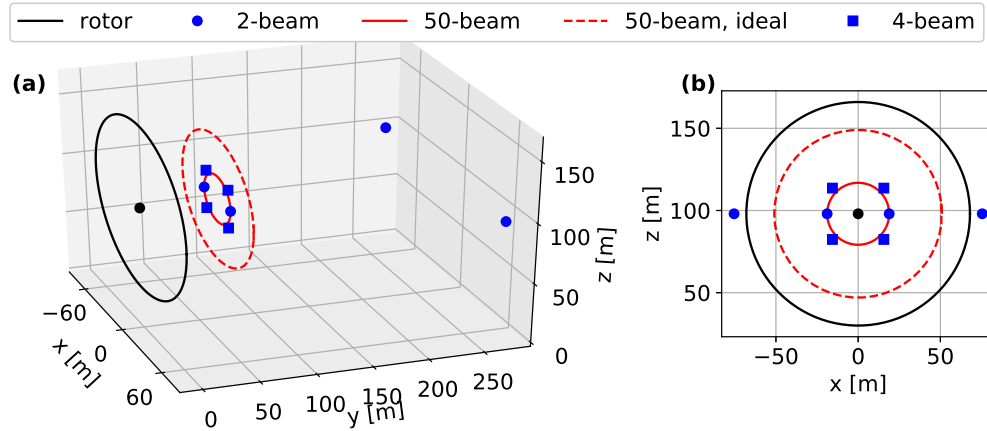
Figure 3. Illustrations of the rotor and lidar measurement points at both 2 and 0.5D with three- and two-dimensional views in (a) and (b), respectively. The *black circle* indicates the location of the lidar

where n_j^i is the j-th component of the unit vector n^i indicating the direction of the i-th beam, v_r^i is the radial velocity retrieved from the i-th beam and u_j is the j-th component of the horizontal wind velocity, whose magnitude is $U_{\text{lidar}} = \sqrt{u_x^2 + u_y^2}$. We do not simulate the lidar probe volume, which is important for turbulence estimations using lidars (Peña et al., 2017; Fu et al., 2022). Therefore, the radial velocities are retrieved as point measurements with a three-dimensional linear interpolation from the flow solution.

When using lidars with more than 2 beams, i.e., the two 50-beam and the 4-beam, we neglect both the lateral and vertical components of the wind speed vector by assuming $u_x = u_z = 0$ m/s, so that the horizontal wind speed at each beam location is retrieved as $u_y = v_r/n_y$. Then, the lidar-estimated disk velocity is obtained as the mean of the beam measurements: $U_{\text{disk,lidar}} = 1/n_{\text{beam}} \sum_{i=1}^{n_{\text{beam}}} u_y^i$. When using the 2-beam lidar focused at 0.5D, the horizontal wind speed at hub height is used as $U_{\text{disk,lidar}}$.

4 Power performance measurement of the first-row turbines

Wind farm blockage affects the flow upstream of the wind farm, impacting the velocity relative to the flow upstream of the isolated turbine. Figure 4-(a) shows the difference between the wind speed $U_{\text{mast}}^{\text{I}}$ measured in front of the isolated turbine and the wind speed $U_{\text{mast}}^{\text{WF}}$ measured in front of the ith wind-farm turbine for the same j^{th} wind direction:

$$\Delta U_{ij} = 100 \frac{U_{\text{mast}}^{\text{WF}}(T_i, \theta_j) - U_{\text{mast}}^{\text{I}}(\theta_j)}{U_{\text{mast}}^{\text{I}}(\theta_j)}. \tag{4}$$

The error bars of Fig. 4-(a) indicate mean and standard deviations associated with the mast orientation α. For most of the
first-row turbines, the measured wind speed is lower than that of the isolated case for all the simulated wind directions, with
velocity reductions sometimes more than 3% in the centre of the row. However, in cases of highly skewed inflow, the wind
speed is increased around the most downwind turbines. For $\theta = 44°$, $U_{\mathrm{mast}}^{\mathrm{WF}}$ at T81 is $\approx 1.5\%$ higher than $U_{\mathrm{mast}}^{\mathrm{I}}$. The same
trend of wind speed variations for a skewed inflow was found by Sebastiani et al. (2022) for a single row of wind turbines,
where the downstream turbines are in the speed-up region formed at the edge of the wakes from the upstream turbines (Meyer
Forsting et al., 2017). In our case, due to the size of the wind farm, the wind speed increase might be also due to the speed-up
at the edge of the wind-farm induction region. The asymmetry in global-blockage effect between cases with almost symmetric
inflow angles, such as $-46°$ and $44°$, is probably due to the asymmetry introduced by the vertical wind veer and wake rotation.
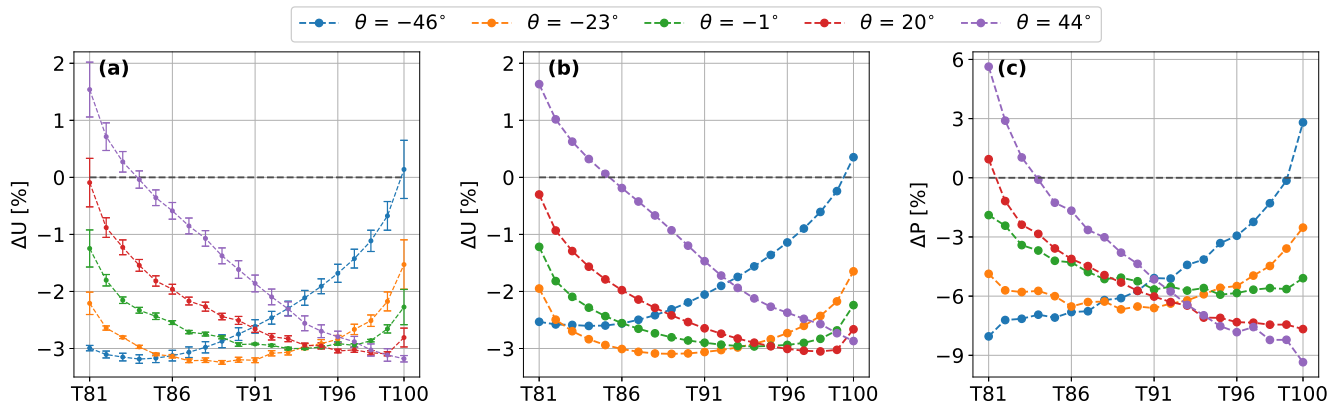
Figure 4. Variations in wind speed (a, b) and power output (c) relatively to the isolated turbine for all the simulated wind directions, when
measuring the wind speed at 2D in front of the turbines with either masts (a) or the 2-beam lidar (b). Error bars in (a) indicate the standard
deviations related to the variation of α.

The blockage-induced velocity variations do not change much when replacing the masts with a 2-beam nacelle-mounted
lidar, as shown in Fig. 4-(b). However, the nacelle lidars measure the wind speed along the rotor axis irrespective of θ, removing
the variation associated with α.

Similarly to the wind speed variations shown in Figs. 4-(a) and (b), Fig. 4-(c) shows the power deviations of the first-row
turbines relatively to the isolated turbine:

$$\Delta P_{ij} = 100 \, \frac{P^{\mathrm{WF}}(T_i, \theta_j) - P^{\mathrm{I}}(\theta_j)}{P^{\mathrm{I}}(\theta_j)}. \tag{5}$$

Since the power output is related to the velocity to the power of 2–3, power variations are larger in magnitude than the velocity
ones, with variations from -9.4% to $+5.6\%$ with respect to the isolated turbines. Additionally, the largest power losses are not
found for the central turbines as for the wind speed, but for the most upstream turbines in the case of strongly skewed inflows,
i.e., T81 for $\theta = -46°$ and T100 for $\theta = 44°$.

Since $U_{\mathrm{mast}}^{\mathrm{WF}}$ and P are not perfectly correlated, their blockage-induced variations cause uncertainty in the power curve, as shown in Fig. 5-(a), which shows the power output from the first-row turbines as function of the wind speed measured by their

220 mast for all wind directions. When applying the correction in Eq. (1) to $U_{\mathrm{mast}}^{\mathrm{WF}}$, the scatter in the power curve does not decrease much, as shown in Fig. (5)-(b). On the other hand, when further correcting $U_{\mathrm{mast}}^{\mathrm{I,rec}}$ with Eq. (2), the scatter in the power curve decreases substantially to a much lower level as shown in Fig. 5-(c).
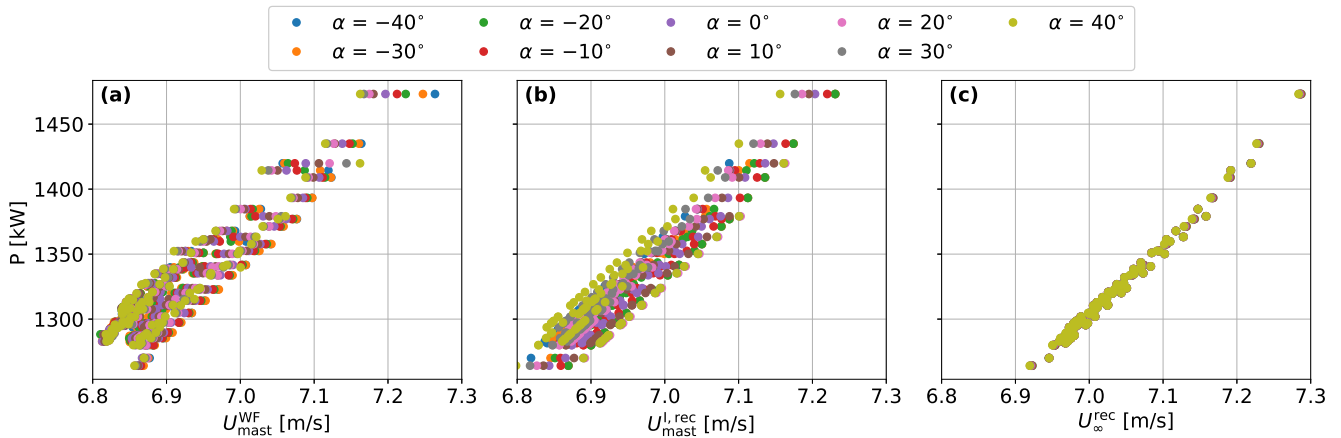
Figure 5. Power output against the mast-measured wind speed of all the first-row turbines for all wind directions and mast locations. (a): no correction applied on the measured wind speed. (b): wind speed corrected with Eq. (1). (c): wind speed corrected with Eq. (2).

The scatter shown in Fig. 5-(a) is not only due to wind farm blockage, but also to the induction/blockage of the test turbine, whose effect is not accounted for using Eq. (1), which reconstructs the wind speed that would be measured around the isolated

225 turbine that is producing the same amount of power as the wind-farm turbine. Since the blockage-induced velocity field is not spatially uniform, the ratio $(U_{\mathrm{mast}}/U_{\mathrm{disk}})^{\mathrm{I}}$ varies with both θ and α as shown in Fig. 6, where error bars represent the standard deviations of the values obtained for different mast orientations α.

When applying Eq. (2), we are correcting for the induction of the test turbine, relating the power output to the freestream velocity that would be measured at the isolated turbine location if the turbine was not there. The power curves retrieved from

230 different masts collapse onto each other, as the freestream velocity does not vary substantially with either α or θ due to the nearly homogeneous velocity field. As shown in Fig. 6, the variation of $(U_{\infty}/U_{\mathrm{disk}})^{\mathrm{I}}$ with α is almost non-existing while a maximum variation of 0.25% is observed with θ. The larger variation with θ is partly due to small variations in the wind profiles among different simulations, as U_{∞} is evaluated at hub height while U_{disk} depends on the wind speed along the entire rotor swept area. Additionally, other factors might cause the discrepancy in $(U_{\infty}/U_{\mathrm{disk}})^{\mathrm{I}}$ between different simulations, such

235 as slight variations in the wake diffusion or number of cells across the disk.

Figure 7 shows scatter plots of the power output against the lidar-retrieved wind speeds for the first-row turbines. When using nacelle lidars, α can be disregarded and the power performance variations are due to the turbine location and wind direction only. The scatter is almost completely reduced by using Eq. (1), as nacelle lidars measure the wind along the rotor

WIND
ENERGY
SCIENCE
DISCUSSIONS
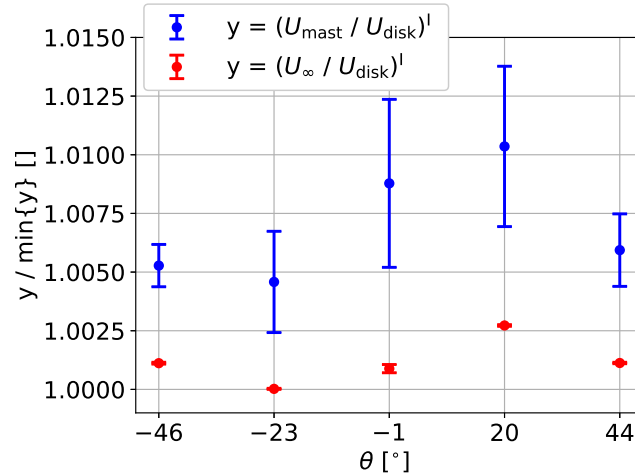
Figure 6. Wind speed variations in the induction zone of the isolated turbine when using mast measurements. Error bars represent the standard deviations of the values obtained for different mast orientations α and same wind direction θ.

axis regardless of θ so that the measurements are equally affected by turbine blockage for different values of θ. When using Eq.
240 (2) to correct for turbine blockage, the scatter does not decrease and the only effect is the shift towards higher velocity values.
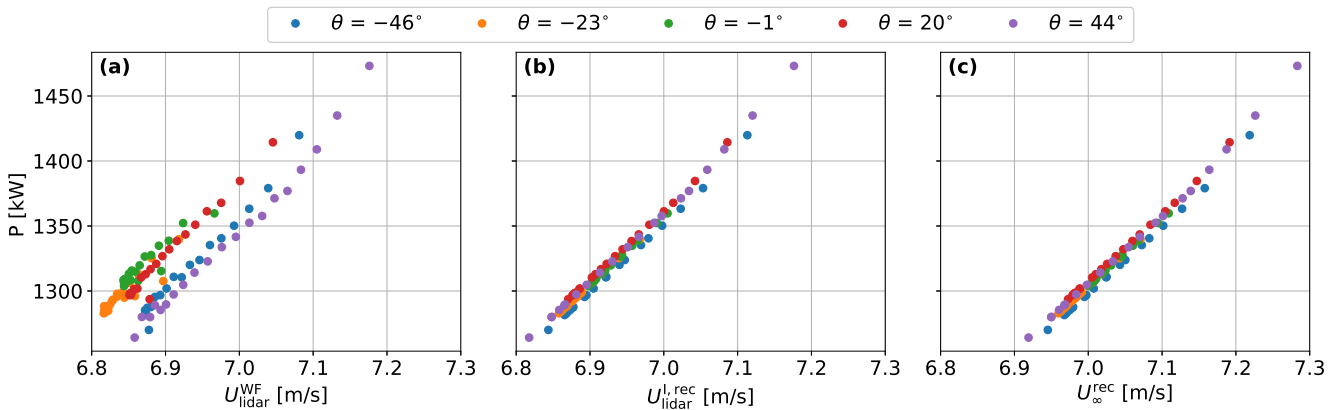
Figure 7. Power output against the lidar-measured wind speed of all the first-row turbines for all wind directions. (a): no correction applied on the measured wind speed. (b): wind speed corrected with Eq. (1). (c): wind speed further corrected with Eq. (2).

Figure 8 shows the variations with θ of the ratios $(U_{\text{lidar}}/U_{\text{disk}})^{\text{I}}$ and $(U_{\infty}/U_{\text{disk}})^{\text{I}}$. Both ratios show almost the same dependency on θ, which demonstrates that the differences in $U_{\text{lidar}}^{\text{I}}$ values are due to the variation of the freestream flow rather than to turbine blockage. This also explains the similarity in the scatter of the power curve when using either $U_{\text{lidar}}^{\text{I,rec}}$ or U_{∞}^{rec}. When measuring power curves with nacelle lidars, Eq. (1) can be used to correct wind-farm effects and retrieve the power
245 performance of the isolated turbine as a function of measured wind speed. However, Eq. (2) is still needed to get the power

output as function of the freestream velocity and to avoid an overestimation of the power performance, as it can be noticed in Fig. 7-(c), where power values are shifted to higher wind speed values compared to Fig. 7-(b).
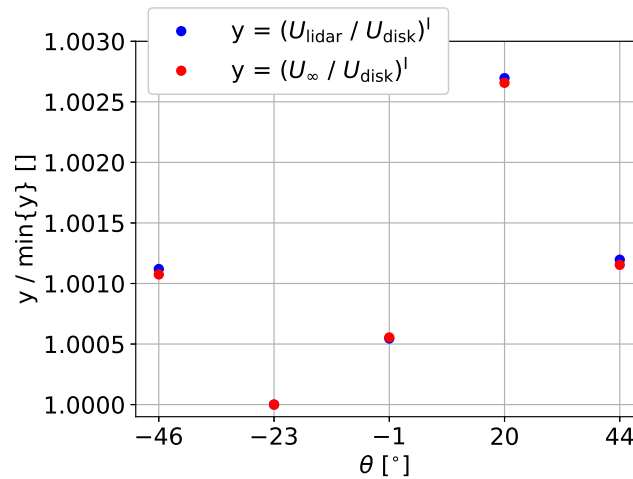
Figure 8. Wind speed variations in the induction zone of the isolated turbine when using nacelle lidars

Figure 9 shows the distributions of the C_P values estimated using the different wind speed definitions. When looking at the C_P of the isolated turbine, we notice lower variation using lidar than mast measurements, as we avoid dependencies on

250 α variations, so that the spread of the C_P values is lower when using $U_{\text{lidar}}^{\text{WF}}$, $U_{\text{lidar}}^{\text{I,rec}}$ and $U_{\text{lidar}}^{\text{I}}$ than with $U_{\text{mast}}^{\text{WF}}$, $U_{\text{mast}}^{\text{I,rec}}$ and $U_{\text{mast}}^{\text{I}}$, respectively. If we assume $C_P = C_P(U_{\text{lidar}}^{\text{I}})$ as the reference value, the C_P estimation is both inaccurate and imprecise when using either $U_{\text{lidar}}^{\text{WF}}$ or $U_{\text{mast}}^{\text{WF}}$. A variation of more than 6% is observed among the C_P values estimated with $U_{\text{mast}}^{\text{WF}}$. The C_P mean values are 1.5% and 1.4% higher than $C_P(U_{\text{lidar}}^{\text{I}})$ for $U_{\text{mast}}^{\text{WF}}$ and $U_{\text{lidar}}^{\text{WF}}$, respectively, whereas the interquartile range (IQR) is 600% and 700% higher for $U_{\text{mast}}^{\text{WF}}$ and $U_{\text{lidar}}^{\text{WF}}$, respectively. By correcting with Eq. (1), the term $U_{\text{mast}}^{\text{I,rec}}$ provides higher

255 accuracy than $U_{\text{mast}}^{\text{WF}}$ with both median and mean values closer to the reference, but the values are still highly spread due to the variations in $(U_{\text{mast}}/U_{\text{disk}})^{\text{I}}$, as shown in Fig. 6. On the other hand, we observe both an increase in accuracy and reduction in the spread when using $U_{\text{lidar}}^{\text{I,rec}}$, with differences with the reference of 0.4% and 19.8% for the mean value and IQR, respectively. However, without applying Eq. (2), the C_P values are not an accurate estimation of the power performance as $C_P = C_P(U_\infty)$. As shown in Fig. 9, the C_P is overestimated relative to $C_P(U_\infty)$ by 4.1% and 4.5% when using $U_{\text{mast}}^{\text{I}}$ and $U_{\text{lidar}}^{\text{I}}$, respectively.

260 On the other hand, the C_P estimation is very accurate when using Eq. (2), with deviations of 0.4% from $C_P(U_\infty)$ for both $U_{\text{mast}}^{\infty,\text{rec}}$ and $U_{\text{lidar}}^{\infty,\text{rec}}$.

It should be noted that the overestimation of C_P observed with both $U_{\text{mast}}^{\text{WF}}$ and $U_{\text{lidar}}^{\text{WF}}$ might have strong implications on the accuracy of AEP estimations. Additionally, the wind speeds corresponding to the high C_T values assumed in this work are usually among the most frequent wind speed values at typical wind farm sites (Hasager et al., 2006). Therefore, the results in

265 Figs. 5, 7 and 9 show the need to correct for the effect of blockage on power performance measurements.
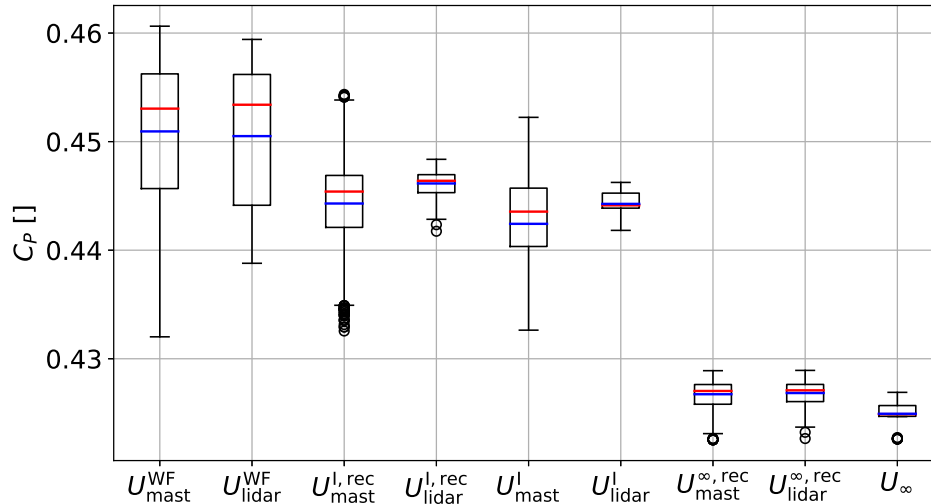
Figure 9. Box plots of the C_P distributions for all wind directions and mast positions for the first-row turbines ($U_{\mathrm{mast}}^{\mathrm{WF}}$, $U_{\mathrm{lidar}}^{\mathrm{WF}}$, $U_{\mathrm{mast}}^{\mathrm{I,rec}}$, $U_{\mathrm{lidar}}^{\mathrm{I,rec}}$, $U_{\mathrm{mast}}^{\infty,\mathrm{rec}}$, $U_{\mathrm{lidar}}^{\infty,\mathrm{rec}}$) and for the isolated turbine ($U_{\mathrm{mast}}^{\mathrm{I}}$, $U_{\mathrm{lidar}}^{\mathrm{I}}$, U_{∞}). Box plot features: quartiles $q1$ and $q3$ (*box limits*); lowest and highest values within $[q1-2\,\mathrm{IQR}, q3+2\,\mathrm{IQR}]$ (*whiskers*); values outside the range $[q1-2\,\mathrm{IQR}, q3+2\,\mathrm{IQR}]$ are shown as outliers (*circles*); median (*red line*) and mean (*blue line*).

5   Lidar-based estimation of the disk velocity

We simulate the 2-beam lidar focused at 19 different distances from the rotor, as shown in Fig. 10-(a). Specifically, we simulate measurements from the rotor plane up to 1.875D, and compute $U_{\mathrm{disk,lidar}}$ from the radial velocities of the two beams at each distance. We then show the correlation between $U_{\mathrm{disk,lidar}}$ and U_{disk} by implementing least-square linear regressions using the

270   ($U_{\mathrm{disk,lidar}}$,U_{disk}) values from all the 20 upstream turbines. The coefficients of determination R^2 of the regressions are shown in Fig. 11.

As it can be noted in Fig. 11, R^2 is low when measuring closer than 0.2D to the rotor and reaches its maximum at 0.25D, with a smooth decreasing trend for further distances. The value at $\Delta y = 0.625$ D appears as an outlier due to numerical biases because the focus point of the beams is at the edge of the highly discretized region (Fig. 10-b). The correlation between U_{disk}

275   and $U_{\mathrm{disk,lidar}}$ decreases very close to the rotor. This is due to a combination of discretisation and interpolation errors. As shown in Fig. 10-(a), the flow field close to the rotor ($y \lesssim 0.2$D) is not as smooth as that far from the rotor. Strong velocity gradients near the rotor, caused by the applied turbine forces, increase discretisation and interpolation errors in this region.

We use the distance of $\Delta y = 0.5$D for testing the correction method based on the work by Troldborg and Meyer Forsting (2017), who showed that the induction zone is self-similar beyond 0.5D upstream of the rotor, i.e., that the induced velocity field

280   is only function of the total C_T with no dependency on the distribution of loads across the rotor. When measuring $U_{\mathrm{disk,lidar}}$
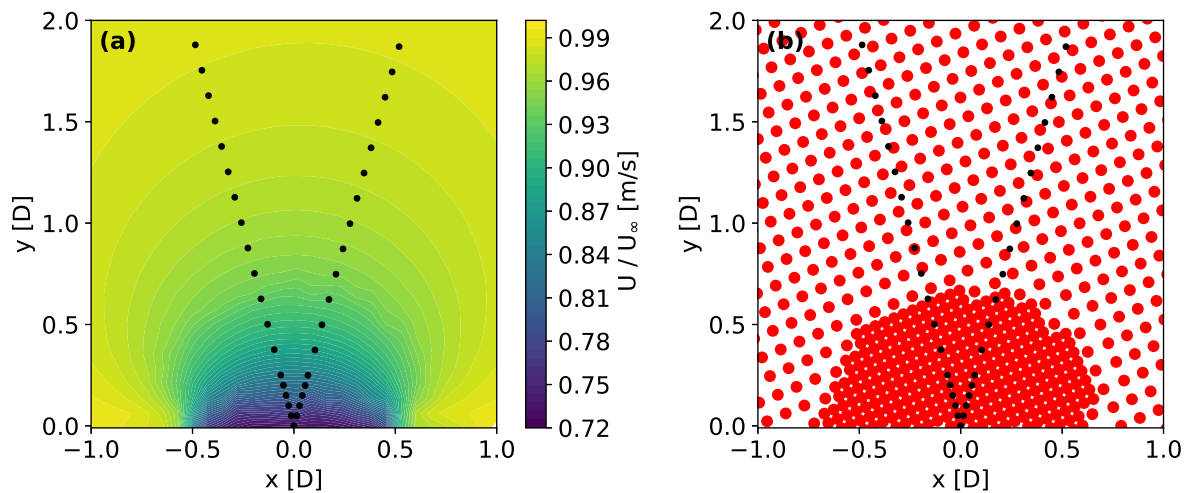
Figure 10. Normalized velocity field at hub height in front of the isolated turbine (a) and grid discretization within the same area (b).
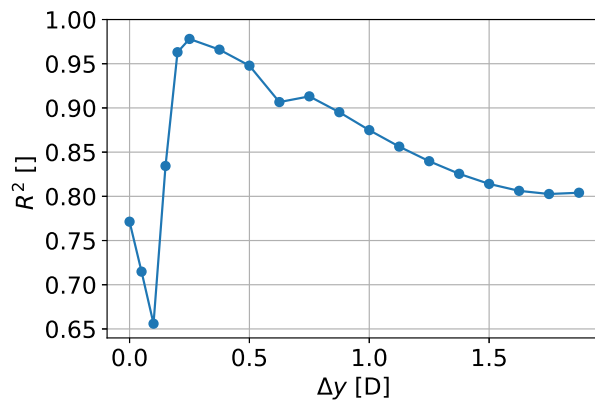
Figure 11. Variation of the coefficient of determination R^2 of the least-square linear regression between U_{disk} and $U_{\mathrm{disk,lidar}}$ for several upstream distances.

at 0.5D, the results are representative of all wind turbine rotors, while using closer measurements might provide results which are representative of the simulated rotor only.

6 Power performance measurements in wakes

The correction method is not limited to blockage effects. In theory, it can be used to correct for any turbine-related disturbances, including wakes. Figure 12 shows the relation between wind speed and power output for all the 100 turbines in the farm and for all the simulated wind directions. We only consider nacelle lidars for power performance measurements of turbines T1, ..., T80. As shown in Fig. 12-(a), the power output is very poorly correlated with the hub-height wind speed measured at 2D in front of the rotor, as this does not represent well U_{disk}. This is due to the complex inflow conditions particularly faced by the downstream turbines (T1, T2, ..., T80), with both axial and lateral velocity gradients affecting the relationship between the measured wind speed and U_{disk}. Additionally, for skewed wind directions, the measurement location might be in wake, while the rotor is not, or the rotor might be partially in wake, further decreasing the correlation between the power output and the measured wind speed.

When applying Eq. (1), as shown in Fig. 12-(b), the corrected wind speed is highly correlated with the power output, as the correlation between U_{disk} and P is not affected by the complexity of the flow field in the model. When further correcting with Eq. (2), as shown in Fig. 12-(c), the scatter in the power curve is not further decreased, and a shift towards slightly higher wind speed values is observed due to the correction of the turbine blockage. When comparing to the freestream power curve values (U_{∞}, P^I) given by the combination of the isolated and freestream simulations (black squares in Fig. 12), we notice an overestimation of the power performance when correcting with Eq. (1) only, and strong agreement with all the turbines' power output when further correcting with Eq. (2).

Figure 12 includes freestream power curve values derived from an additional set of isolated and freestream simulations run at a hub-height wind speed of approximately 6.5 m/s, i.e. around 10% lower than the freestream velocity in the wind farm case. As shown in Fig. 12-(c), after applying the correction, the power curve obtained under waked conditions agrees with the freestream power curve values(U_{∞}, P^I) obtained at lower freestream wind speeds. Such agreement confirms that, under the simulated conditions, the $(U_{\mathrm{mast}}/U_{\mathrm{disk}})^I$ ratio can be assumed as constant over the plateau of the thrust-coefficient curve for wind speed variations up to at least 10%.

The correction method also works well when replacing the term U_{disk} in Eq. (1) with $U_{\mathrm{disk,lidar}}$ retrieved at 0.5D in front of the rotors, as shown in Fig. 13. Although the scatter is slightly larger than when using U_{disk}, all lidar configurations allow for large improvements in the power curve. The results for the three commercial lidars in Fig.13-(a,b,c) are quite similar with no significant improvements when increasing the number of beams, while keeping the same opening angle ($\varphi = 15°, 18°$). However, when increasing φ to $37°$, the correction results in significant less scatter, as shown in Fig. 13-(d). This suggests that $U_{\mathrm{disk,lidar}}$ provides a better estimation of U_{disk} when increasing the scanned area.

The short-range lidar measurements at 0.5D in front of the rotor do not provide an accurate estimation of U_{disk}. However, the measurements at 0.5D can be used to apply the correction method as they are highly correlated with the velocity at the disk
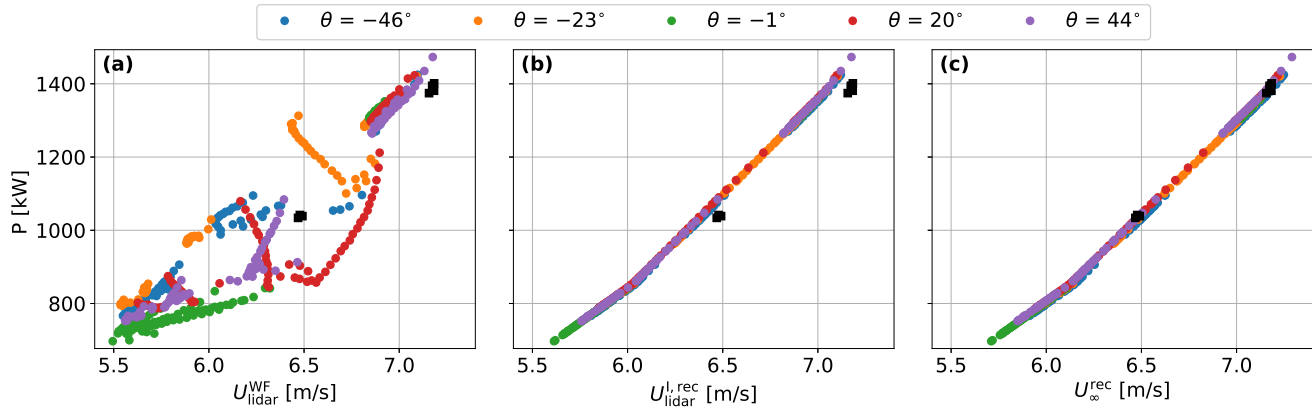
Figure 12. Power output against the lidar-measured wind speed of all the wind-farm turbines for all wind directions. (a): no correction applied on the measured wind speed. (b): wind speed corrected with Eq. (1). (c): wind speed corrected with Eq. (2). Black squares indicate points with the combination (U_∞, P^I) from the isolated and freestream simulations.

(U_{disk}), as shown in Fig. 14. Since the lidar measures very close to the rotor, the correlation between $U_{\text{disk,lidar}}$ and U_{disk} is not greatly impacted by the velocity gradients in the wake, and measurements and rotors might be both either inside or outside the wake. In agreement with the results in Fig. 13, $U_{\text{disk,lidar}}$ estimated from the circular scanning lidar measurements with $\varphi = 37°$ shows the highest correlation with U_{disk} with a coefficient of determination $R^2 = 0.998$.

7 Practical application and limitations

Our results show that the correction method can potentially reduce both bias and uncertainty of power performance measurements. However, the approach relies on the accuracy of the flow model, which might introduce errors when applying the correction to field measurements. In addition, a large number of simulations may be required, given the potential sensitivity of $(U_{\text{disk}}/U_{\text{lidar}})^{\text{WF}}$ to wind direction and the sensitivity of the correction factors to wind speed outside the constant-C_T region of the C_T curve.

The drawbacks of relying exclusively on numerical simulations to make the corrections could be mitigated by complementing the flow model with nacelle lidar measurements. Our numerical results indicate that short-range nacelle lidar measurements can be used to reduce the impact of turbine-induced flow disturbances on power performance measurements, which improves both accuracy and precision on the derived power curve. However, when using nacelle lidar measurements together with Eq. (1), the power performance would be still overestimated because of the difference between $U_{\text{lidar}}^{\text{I}}$ and U_∞. In order to retrieve the freestream power curve $P = P(U_\infty)$, the lidar measurements must be further corrected with Eq. (2), which can only be used with the output from numerical simulations of both the isolated turbine and the freestream flow field. Thus, as shown in
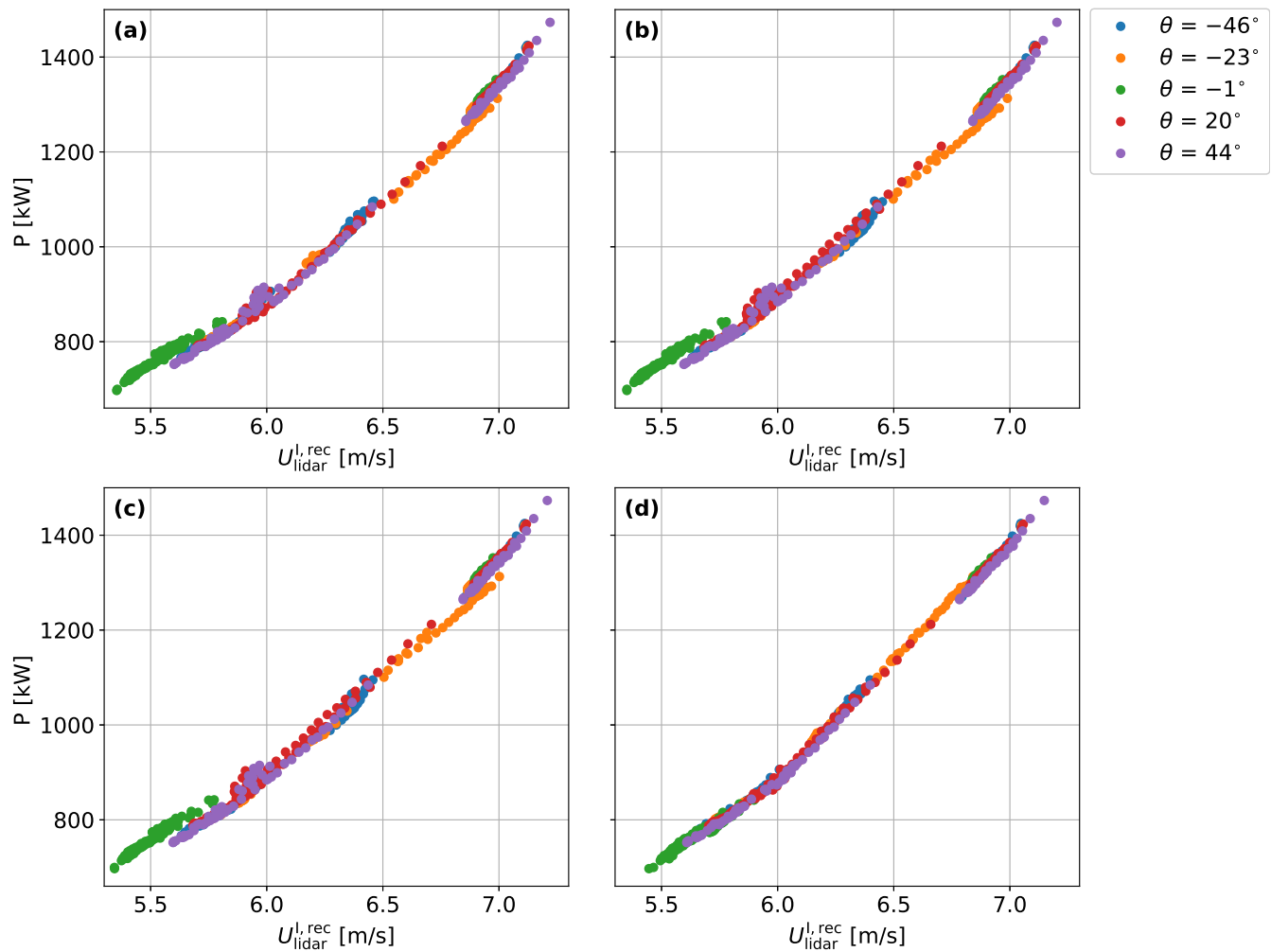
Figure 13. Power output against the lidar-measured wind speed of all the wind-farm turbines and all wind directions. Wind speed measurements are corrected with Eq. (1), where U_{disk} is replaced with the term $U_{\mathrm{disk,lidar}}$, which is estimated using measurements at 0.5D from the 2-beam lidar (a), the 4-beam lidar (b), the 50-beam (c) and the 50-beam ideal lidar (d).
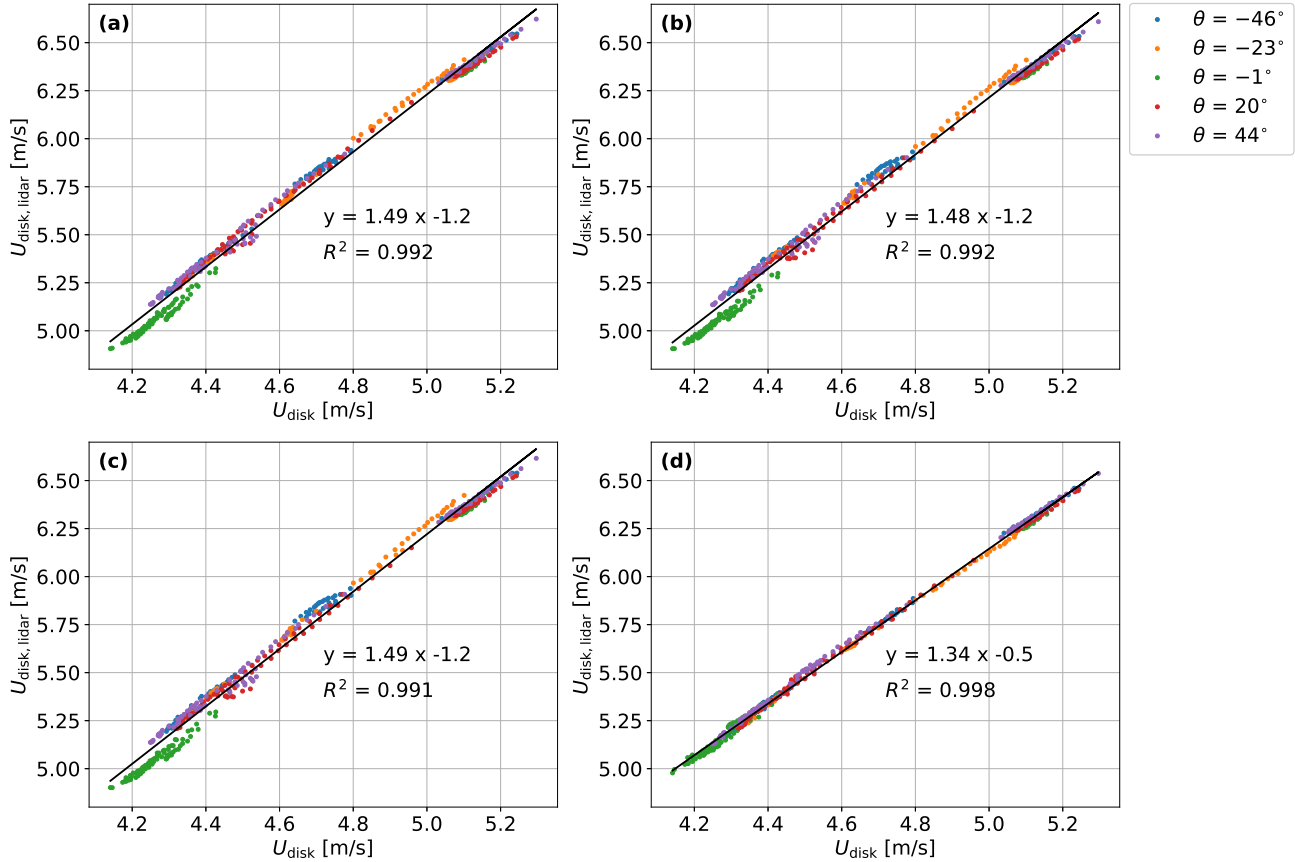
Figure 14. Scatter plots and related linear regressions between U_{disk} and $U_{\text{disk,lidar}}$ estimated with measurements at 0.5D from the 2-beam lidar (a), the 4-beam lidar (b), the CSL (c) and the 50-beam lidar (d).

this work, nacelle lidar measurements can be used to correct for the effect of neighbouring turbines on the measured power performance, but simulations are needed in order to further correct for the blockage effect of the single isolated rotor.

During power performance tests of an isolated turbine, nacelle lidar measurements could be retrieved at both 0.5D and 2D in order to estimate $(U_{\text{disk}}/U_{\text{lidar}})^{\text{I}}$. Then, when power performance tests of the same turbine model are carried out in a wind

335   farm, the ratio $(U_{\text{disk}}/U_{\text{lidar}})^{\text{WF}}$ can be retrieved with the same procedure and the measured power curve can be corrected with Eq. (1). However, $(U_{\text{disk}}/U_{\text{lidar}})^{\text{I}}$ might be sensitive to site-specific effects, e.g., atmospheric stability conditions, which might be different at the isolated turbine location compared to at the wind farm site. In our numerical tests, both the isolated turbine and the wind farm operate under the same atmospheric conditions. This might improve the results compared to the case where measurements are obtained from different sites.

340   Numerical and experimental investigations (Meyer Forsting, 2017; Simley et al., 2016) showed that the induction factor $a = (U_\infty - U_{\text{disk}})/U_\infty$ is not affected by moderate vertical velocity shear, while strong variations of both a and C_T have been

observed under extreme vertical shear conditions with a power law exponent of 0.5 (Meyer Forsting et al., 2018). On the basis of such results, the variation of $(U_{\mathrm{disk}}/U_{\mathrm{lidar}})^{\mathrm{I}}$ among different sites is likely small when measuring under neutral or nearly-neutral conditions, while variations might be observed under stable conditions characterized by strong vertical shear.

345 However, further investigation is needed to evaluate the sensitivity of the correction method to different vertical wind profiles and atmospheric conditions.

Also, the reliability of the correction method under waked conditions could be tested by conducting power performance measurements at the wind farm edge using nacelle lidar measurements. Depending on the wind direction, the reference turbine would be either the most upwind or downwind of the farm. So, $(U_{\mathrm{disk}}/U_{\mathrm{lidar}})^{\mathrm{I}}$ and $(U_{\mathrm{disk}}/U_{\mathrm{lidar}})^{\mathrm{WF}}$ could be retrieved from

350 wake-free and waked measurements, respectively. Equation (1) would be then applied to the waked measurements to evaluate whether they provide a power curve that is consistent with that obtained from the IEC-compliant wake-free measurements.

8   Conclusions

In this work we present and evaluate a method to correct for the impact of turbine-induced flow disturbances on power performance measurements. The correction method is designed to recover the test turbine freestream power curve, i.e. a power curve

355 that faithfully represents turbine power production as a function of freestream wind speed when it is operating in isolation. The method accounts for both the induction of the test turbine as well as the influence of surrounding turbines via blockage and sometimes wakes. Essentially, we take each wind speed value of the measured power curve and correct it to represent the freestream wind speed that would prevail if the test turbine were producing the same amount of power while operating in isolation.

360 Our CFD analysis suggests that the corrections can reduce uncertainty and bias in power performance measurements. Simulations of power performance measurements at a 100-turbine wind farm revealed variations in "measured" C_P of more than 6% along the front row of turbines due to blockage effects. There was also a C_P bias of 4.5%, primarily related to the impact of induction from the test turbine on the measured wind speed. The correction method was shown to reduce these sources of variance and bias in the measured performance. The CFD analysis further demonstrated the potential to correct for much larger

365 variances related to wakes.

The correction factors in this work derive from flow model output, and the same could be done when applying the methodology to real power performance measurements. That said, evidence from this study suggests that the correction factors, at least in part, could also derive from lidar measurements. Measurements taken just 0.5D upstream of the turbine are expected to be highly correlated with power output, much more so than 2.5D upstream, and the CFD analysis indicates that the correction

370 factor related to the influence of surrounding turbines can be reasonably approximated using such near-turbine measurements.

Blockage effects appear to materially distort the outcome of IEC standard power performance measurements; reliable corrections to these effects would reduce uncertainty and produce curves that are more consistent with how power curves are defined and used in energy yield analyses. With this goal in mind, the next step in this research should be to test the correction

methodology on a set of real-world power performance measurements. Field observations could further clarify the validity and
375 utility of these corrections.

Code and data availability. Code and data related to this work might be obtained by contacting the authors.

Author contributions. AS, JB and AP participated in the conceptualization and design of the work. AS, JB and AP participated to regular
discussions on the interpretation of the results. JB theoretically defined the correction method and performed the CFD simulations. AS
defined the lidar-based application of the method and conducted the post-process analysis of the CFD results, retrieving the virtual lidar
380 measurements. AS wrote the draft manuscript. JB and AP supported the whole analysis and reviewed and edited the manuscript.

Competing interests. The authors declare that they have no conflict of interest.

Acknowledgements. This work has received funding from the European Union Horizon 2020 through the Innovation Training Network Marie
Skłodowska-Curie Actions: Lidar Knowledge Europe (LIKE) [grant number 858358].

References

385 Allaerts, D. and Meyers, J.: Boundary-layer development and gravity waves in conventionally neutral wind farms, Journal of Fluid Mechanics, 814, 95–130, https://doi.org/10.1017/jfm.2017.11, 2017.

Bleeg, J.: A Graph Neural Network Surrogate Model for the Prediction of Turbine Interaction Loss, Journal of Physics: Conference Series, 1618, https://doi.org/10.1088/1742-6596/1618/6/062054, 2020.

Bleeg, J., Digraskar, D., Horn, U., and Corbett, J.: Modelling stability at microscale, both within and above the atmospheric boundary layer,
390   substantially improves wind speed predictions, In Proceedings of the EWEA Conference, Paris, France, 2015a.

Bleeg, J., Digraskar, D., Woodcock, J., and Corbett, J.-F.: Modeling stable thermal stratification and its impact on wind flow over topography, Wind Energy, 18, 369 – 383, https://doi.org/10.1002/we.1692, 2015b.

Bleeg, J., Purcell, M., Ruisi, R., and Traiger, E.: Wind farm blockage and the consequences of neglecting its impact on energy production, Energies, 11, https://doi.org/10.3390/en11061609, 2018.

395 Branlard, E. and Meyer Forsting, A.: Assessing the blockage effect of wind turbines and wind farms using an analytical vortex model, Wind Energy, 23, 2068–2086, https://doi.org/10.1002/we.2546, 2020.

Ebenhoch, R., Muro, B., Dahlberg, J.-, Berkesten Hägglund, P., and Segalini, A.: A linearized numerical model of wind-farm flows, Wind Energy, 20, 859 – 875, https://doi.org/10.1002/we.2067, 2017.

Fu, W., Sebastiani, A., Peña, A., and Mann, J.: Dependence of turbulence estimations on nacelle-lidar scanning strategies, Wind Energy
400   Science Discussions, 2022, 1–21, https://doi.org/10.5194/wes-2022-85, 2022.

Hasager, C. B., Barthelmie, R. J., Christiansen, M. B., Nielsen, M., and Pryor, S. C.: Quantifying offshore wind resources from satellite wind maps: study area the North Sea, Wind Energy, 9, 63–74, https://doi.org/https://doi.org/10.1002/we.190, 2006.

IEC: 61400-12-1, Power performance measurements of electricity producing wind, turbines, 2017.

McTavish, S., Rodrigue, S., Feszty, D., and Nitzsche, F.: An investigation of in-field blockage effects in closely spaced lateral wind farm
405   configurations, Wind Energy, 18, 1989–2011, https://doi.org/10.1002/we.1806, 2015.

Medici, D., Ivanell, S., Dahlberg, J.-A., and Alfredsson, P. H.: The upstream flow of a wind turbine: blockage effect, Wind Energy, 14, 691–697, https://doi.org/10.1002/we.451, 2011.

Meyer Forsting, A.: Modelling Wind Turbine Inflow: The Induction Zone, Ph.D. thesis, Denmark, https://doi.org/10.11581/DTU:00000022, 2017.

410 Meyer Forsting, A., Troldborg, N., and Gaunaa, M.: The flow upstream of a row of aligned wind turbine rotors and its effect on power production, Wind Energy, 20, 63–77, https://doi.org/10.1002/we.1991, 2017.

Meyer Forsting, A., Van Der Laan, M., and Troldborg, N.: The induction zone/factor and sheared inflow: A linear connection?, Journal of Physics: Conference Series, 1037, https://doi.org/10.1088/1742-6596/1037/7/072031, 2018.

Nishino, T. and Draper, S.: Local blockage effect for wind turbines, Journal of Physics: Conference Series, 625, https://doi.org/10.1088/1742-
415   6596/625/1/012010, 2015.

Nygaard, N. and Brink, F.: Measurements of the wind turbine induction zone, vol. 26-29 June 2017, 2017.

Nygaard, N. G., Steen, S. T., Poulsen, L., and Pedersen, J. G.: Modelling cluster wakes and wind farm blockage, Journal of Physics: Conference Series, 1618, https://doi.org/10.1088/1742-6596/1618/6/062072, 2020.

Peña, A., Mann, J., and Dimitrov, N.: Turbulence characterization from a forward-looking nacelle lidar, Wind Energy Science, 2, 133–152,
420   https://doi.org/10.5194/wes-2-133-2017, 2017.

Sebastiani, A., Peña, A., Troldborg, N., and Meyer Forsting, A.: Evaluation of the global-blockage effect on power performance through simulations and measurements, Wind Energy Science, 7, 875–886, https://doi.org/10.5194/wes-7-875-2022, 2022.

Sebastiani, A., Peña, A., and Troldborg, N.: Numerical evaluation of multivariate power curves for wind turbines in wakes using nacelle lidars, Renewable Energy, 202, 419–431, https://doi.org/https://doi.org/10.1016/j.renene.2022.11.081, 2023.

425 Segalini, A.: An analytical model of wind-farm blockage, Journal of Renewable and Sustainable Energy, 13, https://doi.org/10.1063/5.0046680, 2021.

Segalini, A. and Dahlberg, J. Å.: Blockage effects in wind farms, Wind Energy, 23, 120–128, https://doi.org/10.1002/we.2413, 2020.

Simley, E., Angelou, N., Mikkelsen, T., Sjöholm, M., Mann, J., and Pao, L. Y.: Characterization of wind velocities in the up-stream induction zone of a wind turbine using scanning continuous-wave lidars, Journal of Renewable and Sustainable Energy, 8,

430 https://doi.org/10.1063/1.4940025, 2016.

Strickland, J. M. and Stevens, R. J.: Investigating wind farm blockage in a neutral boundary layer using large-eddy simulations, European Journal of Mechanics, B/Fluids, 95, 303 – 314, https://doi.org/10.1016/j.euromechflu.2022.05.004, 2022.

Troldborg, N. and Meyer Forsting, A.: A simple model of the wind turbine induction zone derived from numerical simulations, Wind Energy, 20, 2011–2020, https://doi.org/10.1002/we.2137, 2017.

435 van der Laan, P., Sørensen, N., Réthoré, P.-E., Mann, J., Kelly, M., and Troldborg, N.: The k-ϵ-fP model applied to double wind turbine wakes using different actuator disk force methods, Wind Energy, 18, 2223–2240, https://doi.org/10.1002/we.1816, 2015.